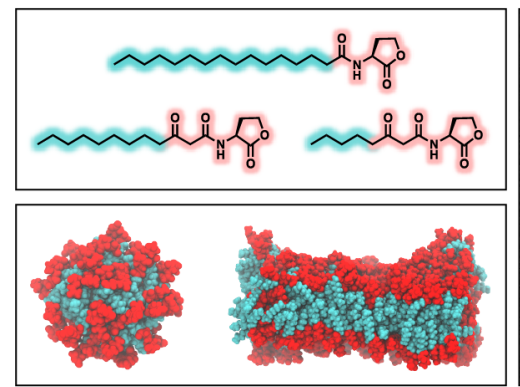
# Bacterial Quorum Sensing Signals Self-Assemble in Aqueous Media to Form Micelles and Vesicles: An Integrated Experimental and Molecular Dynamics Study

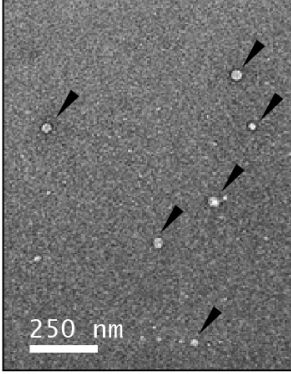
Curran G. Gahan, <sup>1,†</sup> Samarthaben J. Patel, <sup>1,†</sup> Michelle E. Boursier, <sup>2,‡</sup> Kayleigh E. Nyffeler, <sup>2</sup> James Jennings, <sup>1,§</sup> Nicholas L. Abbott, <sup>1,#</sup> Helen E. Blackwell, <sup>2,\*</sup> Reid C. Van Lehn, <sup>1,\*</sup> and David M. Lynn <sup>1,2,\*</sup>

<sup>1</sup>Dept. of Chemical and Biological Engineering, Univ. of Wisconsin–Madison, 1415 Engineering Dr., Madison, WI 53706; <sup>2</sup>Dept. of Chemistry, Univ. of Wisconsin–Madison, 1101 University Ave., Madison, WI 53706, USA; <sup>‡</sup>Current address: Amgen, Inc., 1 Amgen Center Dr., Thousand Oaks, CA 91320; <sup>§</sup>Current address: Department of Chemistry, University of Sheffield, S11 8RZ, United Kingdom <sup>#</sup>Current address: Smith School of Chemical and Biomolecular Engineering, Cornell Univ., Ithaca, NY 14853; <sup>†</sup>Equally contributing author; Email: (H.E.B.) blackwell@chem.wisc.edu; (R.C.V.) vanlehn@wisc.edu; (D.M.L.) dlynn@engr.wisc.edu

ABSTRACT: Many species of common bacteria communicate and coordinate group behaviors, including toxin production and surface fouling, through a process known as quorum sensing (QS). In Gram-negative bacteria, QS is regulated by N-acyl L-homoserine lactones (AHLs) that possess a polar homoserine lactone head group and a nonpolar aliphatic tail. Past studies demonstrate that AHLs can aggregate in water or adsorb at interfaces, suggesting that molecular self-assembly could play a role in processes that govern bacterial communication. We used a combination of biophysical characterization and atomistic molecular dynamics (MD) simulations to characterize the self-assembly behaviors of 12 structurally related AHLs. We used static light scattering and measurements of surface tension to characterize the assembly of four naturally occurring AHLs (3-oxo-C8-AHL, 3-oxo-C12-AHL, C12-AHL, and C16-AHL) in aqueous media and determine their critical aggregation concentrations (CACs). MD simulations and alchemical free energy calculations were used to predict thermodynamically preferred aggregate structures for each AHL. Those calculations predicted that AHLs with 10 or 12 tail carbon atoms should form spherical micelles, and that AHLs with 14 or 16 tail carbon atoms should form vesicles in solution. Characterization of solutions of AHLs using negative stain transmission electron microscopy (TEM) and dynamic light scattering (DLS) revealed aggregates with sizes consistent with spherical micelles or small unilamellar vesicles for 3-oxo-C12-AHL and C12-AHL, and the formation of large vesicles (~250 nm) in solutions of C16-AHL. These experimental findings are in general agreement with our simulation predictions. Overall, our results provide insight into processes of self-assembly that can occur in this class of bacterial amphiphiles and, more broadly, provide a potential basis for understanding how AHL structure could influence processes that bacteria use to drive important group behaviors.

For Table of Contents Use Only:





# Introduction

Quorum sensing (QS) is an intercellular signaling process by which bacteria assess their population densities and coordinate gene expression to regulate group behaviors and adapt to changing environments.<sup>1-2</sup> Outcomes of QS include the production of virulence factors<sup>3</sup> and the formation of bacterial biofilms, both of which can be harmful to humans or costly in commercial and industrial contexts. In many common bacterial pathogens, QS is controlled by the production and dissemination of small-molecule or peptidic signals. 1-2, 4-5 The structures of these signals can vary widely amongst bacterial species and are known to influence the specificity of their interactions with their biomolecular targets through receptor-ligand interactions. 6-11 However, the structures and solution behaviors of QS signals also have the potential to mediate other interactions important to the transport of these molecules in solution, into cells, or through biofilms. In this study, we report fundamental physicochemical characterization and the results of integrated molecular dynamics (MD) simulation studies that provide new insights into the solution behaviors and self-assembly of N-acyl-L-homoserine lactones (AHLs; Figure 1), the most widely characterized signals that regulate QS in Gramnegative bacteria.<sup>5, 7</sup>

AHLs are amphiphilic and possess relatively polar, non-ionic L-homoserine 'head groups' and nonpolar alkyl 'tails'. Many past studies have identified roles that AHLs play in regulating QS in bacteria and have determined the influence of AHL structure on binding to cognate intracellular protein receptors. 12-14 Much of this work has focused on the opportunistic pathogen *Pseudomonas aeruginosa*, which uses both the short-tailed C4-AHL and the long-tailed 3-oxo-C12-AHL (Figure 1) for QS. 1, 5, 7 Although an understanding of the roles that AHLs play in modulating QS is emerging, less is known about how these molecules are transported between

**Figure 1:** Structures of the naturally occurring AHLs examined in this study. AHLs indicated with asterisks were studied experimentally.

cells in solution or within biofilms and the manners by which AHL structure can influence these processes. Kaplan *et al.* reported that AHLs with short tails containing four or six carbon atoms (*e.g.*, C4-AHL) can diffuse freely across bacterial membranes,<sup>15</sup> and Pearson *et al.* have demonstrated that AHLs with longer tails (*e.g.*, 3-oxo-C12-AHL) require active transport to be pumped out of cells (at least in *P. aeruginosa*).<sup>16-17</sup> Classical models of QS also assume that AHLs diffuse freely through the extracellular environment and into neighboring cells. However, AHLs also have the potential to exhibit behaviors such as cooperative self-assembly and surface activity that are common to other conventional amphiphiles, such as surfactants and lipids, which

could enable alternate modes of molecular transport. In support of this view, 3-oxo-C12-AHL and C16-AHL have both been found to be associated with the outer membrane vesicles of various bacterial species, <sup>18</sup> and inhibition of the production of outer membrane vesicles has been reported to inhibit QS. <sup>19</sup> Likewise, Song *et al.* recently reported that bacterial AHLs can insert selectively into lipid rafts found in mammalian cell membranes and trigger processes that lead to apoptosis. <sup>20</sup> These and other related results discussed below suggest that the amphiphilicity of AHLs can facilitate molecular self-assembly and allow them to adsorb or aggregate into nanostructures that could facilitate transport in bacterial communities.

To complement biological assays, model systems have been used to determine if AHLs demonstrate signatures of amphiphilic behavior. Daniels *et al.* reported that C6-AHL, 3-OH-C8-AHL, C10-AHL, C12-AHL and C14-AHL can form monolayers at air/water interfaces that have pressure-area isotherms characteristic of conventional amphiphile films.<sup>21</sup> Davis *et al.* demonstrated using static light scattering that long-tailed AHLs show characteristic signs of aggregation in aqueous buffers above certain critical concentrations that depend, at least in part, upon AHL structure (*e.g.*, tail length).<sup>22</sup> That work also demonstrated using dynamic light scattering (DLS) that 3-oxo-C14-AHL can form aggregates with hydrodynamic diameters of ~20 nm. When combined, those results are consistent with processes of self-assembly, but the hydrodynamic diameters of the aggregates reported by Davis *et al.* were substantially larger than those typically associated with spherical micelles formed by many other single-tailed surfactants,<sup>22</sup> and little is understood about the nanostructures of AHL aggregates or how changes in head and tail group structure could promote changes in aggregate morphology.

These past studies raise many intriguing questions about the roles that supramolecular processes could play in mediating bacterial communication. For example, would the aggregation

of AHLs tend to mute or amplify a signal? Could environmental factors alter such aggregation behavior and thereby serve as a tool with which to tune QS signaling? Could the structures of AHLs be tailored (permanently or transiently)<sup>23</sup> to alter aggregation, and thereby change QS outcomes? As a first step toward providing insight into the potential of AHL aggregation to affect or mediate these biological processes, this current study sought to systematically characterize the impacts of head and tail group structure on the self-assembly of a series of naturally occurring AHLs in defined buffer and in biologically relevant bacterial growth medium. We used two independent biophysical characterization techniques, light scattering and measurements of surface tension, to measure the critical aggregation concentrations (CACs) of some of the most common natural AHLs and characterize the sizes of the nanoscale and microscale aggregates that form in solution. We also characterized the sizes and morphologies of AHL aggregates using transmission electron microscopy (TEM). In combination with these experimental studies, we performed MD simulations to predict the impacts of head group structure and tail length on the thermodynamically preferred aggregate structures formed by these AHLs. The results of alchemical free energy calculations predicted that AHLs containing 10 or more tail carbon atoms should form nanoscale aggregates, with C12-AHL and 3-oxo-C12-AHL preferring to form spherical aggregates around 5 to 6 nm in diameter and C14-AHL, C16-AHL, 3-oxo-C14-AHL, and 3-oxo-C16-AHL preferring to form bilayer vesicles. These MD results and related structure predictions are consistent with the experimental characterization of aggregate size and morphology obtained using DLS and TEM. Overall, our results provide new insights into processes of self-assembly that occur in this important class of non-ionic amphiphiles and provide a potential basis for understanding how the chemical structures of AHLs could influence processes that bacteria use to drive group behaviors such as biofouling and toxin production.

# **Materials and Methods**

Materials. Dimethyl sulphoxide (DMSO) and ethanol were obtained from Fisher Scientific (Pittsburgh, PA). Uranyl acetate (UA), Whatman grade 4 filter paper, and stock 5.0 M sodium hydroxide solution were purchased from Sigma Aldrich (Milwaukee, WI). AHLs were either purchased from Sigma Aldrich or synthesized as previously reported. <sup>12, 24</sup> Syringes (5 mL, 10 mL, and 30 mL) were obtained from Becton Dickinson (Franklin Lakes, NJ). Minisort X plus 0.2 μm syringe filters were acquired from Sartorius Stedim Biotech (Goettingen, Germany). Centrifuge tubes (1.7 mL), were purchased from Axygen products (Tewksbury, MA). DTS1070 folded capillary cuvettes were purchased from Malvern Panalytical (Westborough, MA). Luria-Bertani (LB) medium was obtained from Research Products Industrial (Mt. Prospect, IL). TEM grids (300 Mesh) were purchased from Electron Microscopy Sciences (Haltfield, PA). Deionization of distilled water was performed using a Milli-Q system (Millipore, Bedford, MA) yielding water with a resistivity of 18.2 MΩ. All materials were used as received without further purification unless otherwise specified.

General Considerations. Static and dynamic light scattering measurements were made using a Malvern Zetasizer and 1 cm x 1 cm plastic cuvettes. Zeta potential measurements were made using a Malvern Zetasizer and a DTS1070 folded capillary cell. During light scattering and zeta potential measurements, the detector was placed at an angle of 173° from the 632.8 nm incident laser. Surface tension measurements were acquired using a Nima Type 611 trough with a PS4

pressure sensor (Coventry, England) with Bolin Scientific paper Wilhelmy plates (Bolin Scientific, Gothenburg Sweden) or a Kruss K10T Tensiometer (Matthews, NC) with a platinum Du Noüy ring or Wilhelmy plate. TEM images were acquired using a Techni T12 Microscope and Gatan 4k Ultrascan CCD camera.

Determination of Critical Aggregation Concentrations (CACs). For all experiments, the AHLs were stored in stock solutions at concentrations of 300 mM in DMSO for C4-AHL, C6-AHL and 3-oxo-C8-AHL and 20 mM, 25 mM, and 2 mM in DMSO for, C12-AHL, 3-oxo-C12-AHL, and C16-AHL, respectively. To prepare dilutions of these DMSO stocks to a desired concentration in aqueous solution, the stocks were first diluted in DMSO to 100 times the final aqueous concentration, and then diluted 1:100 into the desired buffer or medium. The solutions were allowed to sit for 30 minutes at the temperature stated for that experiment before characterization of the CAC. All AHL solutions were used within 3 hours of initial dilutions of the DMSO stocks to minimize the potential impact of AHL head group hydrolysis on the CAC.

Static Light Scattering. The CACs of the AHLs were determined by static light scattering by adapting methods described previously.<sup>22</sup> The desired solvent (water or LB medium) was filtered twice and then centrifuged at 2000 RPM for 3 minutes to remove particulates and air bubbles from the buffer. AHL solutions (1.2 mL) were prepared in a 1.7 mL Eppendorf tube. The samples were then centrifuged again at 1500 RPM for 2 minutes to sediment particulates and remove air bubbles, and allowed to sit thereafter in a constant temperature water bath for 30 minutes. Samples dispersed in water were maintained at 30 °C while those in LB medium were maintained at 37 °C. Aliquots (1 mL) of these samples were transferred to a cuvette and the

scattered light intensity was measured three times per sample. Each measurement averaged the intensity of the light scattered by the sample over 5 seconds. Linear regression of increasing scattered light intensity at increasing AHL concentrations was performed and used to determine the CAC of the AHL being tested as described in the Supporting Information.

Measurement of the Surface Tensions of AHL Solutions. Measurements of the surface tensions of AHL solutions were made using a paper Wilhelmy plate or Du Noûy ring by adapting a procedure described previously. Linear regression of decreasing surface tension at increasing concentration of AHLs was used to determine the CACs of the AHLs as described in the Supporting Information. For measurements using a Nima Type 611 trough, the tensiometer was calibrated using an internal calibration program and checked by ensuring the surface tension of distilled, deionized water was near 72 mN/m. A dry paper Wilhelmy plate was immersed in PBS for 10 minutes at room temperature to hydrate before surface tension measurements were made. AHL solutions were prepared as described above and allowed to sit at room temperature, and then the hydrated Wilhelmy plate was dipped into the AHL solution and allowed to sit at the solution interface for 5 minutes. The surface tension ( $\gamma$ ) was determined by measuring the change in force applied to the Wilhelmy plate by the solution while in contact with the solution interface and directly after removing the plate from solution. This change in force (F) was then used in the Wilhelmy equation, F

$$\gamma = \frac{F}{l\cos\left(\theta\right)} \tag{1}$$

where l is the wetted perimeter of the paper Wilhelmy plate (21 mm) and  $\theta$  is the contact angle of water on the Wilhelmy plate, which is assumed to be  $0^{\circ}$  for a paper plate. For measurements made using a Kruss K10T Tensiometer, a platinum Du Noüy ring or Wilhelmy plate was cleaned

using a butane torch and immediately hung from the tensiometer balance. The internal gauge was then zeroed to the weight of the ring or plate. The tensiometer was calibrated by adjusting the balance until a surface tension of ~72 mN/m was recorded for a solution of deionized, distilled water. The ring or plate was then immersed into the AHL solution until the internal motor was enabled and allowed to raise the ring or plate from the solution until the tensiometer balanced. For multiple measurements, the plate or ring was removed from solution, the balance was rezeroed, and the process was repeated.

Characterization of Aggregate Sizes using Dynamic Light Scattering. DLS measurements of AHL solutions were made using a Malvern Zetasizer ZS Nano. Samples of AHLs were prepared at concentrations above their measured CACs in filtered Milli-Q water or LB medium and allowed to stand at 30 °C or 37 °C, respectively, for 30 minutes. Aliquots (1 mL) of the samples were then transferred to a 1 cm x 1 cm plastic cuvette, the cuvette was then placed in the Zetasizer for 2 minutes at the prescribed temperature, and the scattered light intensity was measured. The correlator measured the intensity correlation function for delay times ranging from 2 µs to 200 ms. The hydrodynamic diameters reported assume that the aggregates measured are spherical and diffuse purely by Brownian motion.

Characterization of Zeta Potential. Zeta potential measurements of AHL solutions were made using a Malvern Zetasizer ZS Nano. Samples of AHLs were prepared at concentrations above their measured CACs in filtered Milli-Q water and allowed to stand at 30 °C for 30 minutes. Aliquots (1 mL) of the samples were then transferred to a DTS1070 folded capillary cuvette, the cuvette was placed in the Zetasizer for two minutes at the prescribed temperature, and zeta

potential measurements were performed. The zeta potential of the solution was measured 7 to 10 times per sample and three independent samples were measured. The zeta potentials of the aggregates were calculated using the Smoluchowski model.

Characterization of AHL Aggregates using Transmission Electron Microscopy. Negative staining of AHL solutions for observation by TEM was performed using uranyl acetate (UA) and a procedure used in past studies to characterize self-assembled surfactant aggregates. 26-29 UA stain (2%) was prepared by mixing 100 mg of UA with 5 mL of boiling Milli-Q water for 5 minutes. Sodium hydroxide (20 µL, 5.0 M) was then added to the stain solution and the resulting solution was stirred for another 5 minutes. The solution was filtered through a 0.22 µm filter and stored in the dark prior to use. Immediately before sample staining, two drops (100 µL each) of the UA stain were pipetted on top of a sheet of parafilm. Solutions of AHLs at desired concentrations above their CACs were prepared in water as described previously and allowed to stand at room temperature for 30 minutes. An aliquot (3 µL) of the AHL solution was then pipetted onto a charged 300 mesh Cu TEM grid and allowed to sit for 1 minute. Excess solution was blotted off of the grid using filter paper, and the grid was immediately passed through a drop of stain. Excess stain was then blotted off, and the grid was submerged in another drop of stain for an additional 60 seconds. Excess stain was again blotted off and further removed using suction. The grid was allowed to air dry before being placed in a TEM grid holder. Stained samples were imaged using a Techni T12 TEM at 120 V accelerating voltage at one second exposure time on a Gatan 4k Ultrascan CCD camera.

Simulation Systems and Parameters. Atomistic MD simulations were performed to model the solution behavior and self-assembly thermodynamics of AHLs. Atomistic models were chosen to capture the detailed chemistry of the AHL structures shown in Figure 1, including the difference between AHLs with and without a 3-oxo group. AHL structures were generated using the CHARMM-GUI Ligand Reader & Modeler. 30-31 The CHARMM36 force field was used to model the AHLs with the TIP3P model for water. Two types of simulations were performed: unbiased MD simulations to observe AHL self-assembly, and alchemical free energy calculations to compute the free energy change for aggregation (detailed below). In all simulations, Verlet lists were generated using a 1.2 nm neighbor list cutoff. Van der Waals interactions were modeled with a Lennard-Jones potential using a 1.2 nm cutoff that was smoothly shifted to zero between 1.0 nm and 1.2 nm. Electrostatic interactions were calculated using the smooth Particle Mesh Ewald method with a short-range cutoff of 1.2 nm, grid spacing of 0.12 nm, and 4<sup>th</sup> order interpolation. Bonds were constrained using the LINCS algorithm. Unbiased simulations were performed using a leapfrog integrator with a 2-fs timestep, whereas alchemical free energy calculations were performed using a leapfrog stochastic dynamics integrator with a 2-fs timestep. All simulations were performed using Gromacs 2016.<sup>32</sup>

Initial configurations for the unbiased simulations consisted of AHL molecules placed on a grid spaced by 1.5 nm in each Cartesian direction. Unbiased simulations were performed for 64 C4-AHL molecules and for 64, 216, and 512 3-oxo-C12-AHL molecules. Initial simulation configurations for the alchemical free energy calculations consisted of either a single AHL in water or an AHL aggregate generated using PACKMOL.<sup>33</sup> Five different aggregate structures were generated: three spherical aggregates with 20, 50, and 100 AHL molecules, respectively; cylindrical aggregates with 150 AHL molecules; and bilayers with 128 AHL molecules (oriented

with the normal parallel to the *z*-axis of the simulation box). Each system was solvated in water after preparation. Snapshots of example systems as prepared are shown in the Supporting Information.

All simulation systems were energy minimized using the steepest descent method. The unbiased simulations were performed for 50 ns with the temperature maintained at 37 °C using a Berendsen thermostat with a time constant of 1.0 ps and the pressure maintained at 1 bar using an isotropic Berendsen barostat with a time constant of 5 ps and a compressibility of 4.5×10<sup>-5</sup> bar<sup>-1</sup>. For the alchemical free energy calculations, the energy minimized systems were first equilibrated with the temperature maintained at 37 °C using a Berendsen thermostat with a time constant of 1.0 ps and the pressure maintained at 1 bar using a Berendsen barostat with a time constant of 5 ps and a compressibility of 4.5×10<sup>-5</sup> bar<sup>-1</sup>. An isotropic barostat was used for the equilibration of spherical aggregates, whereas a semi-isotropic barostat was used for the equilibration of bilayers. A more elaborate pressure coupling protocol, involving both a semiisotropic and an isotropic Berendsen barostat, was used for the equilibration of the cylindrical aggregates as detailed in the Supporting Information. Aggregate structures were equilibrated for 50 ns, and the single AHL in water was equilibrated for 5 ns. To confirm that the systems had reached equilibrium, the last 10 ns of each equilibration trajectory were divided into two blocks, then AHL center-of-mass density distributions were computed for each block and compared to ensure no further change in aggregate structure. Further details on this procedure are provided in the Supporting Information.

Alchemical Free Energy Calculation Theory and Implementation. The CAC is related to the free energy change for aggregation,  $\Delta \mu_{aggr}$ , by Equation 2:<sup>34</sup>

$$\Delta\mu_{aggr} = -(\mu_1^o - \mu_N^o) = RT \ln (CAC)$$
(2)

 $\mu_N^o$  is the chemical potential of an amphiphile in an aggregate with aggregation number N (indicating the number of molecules in the aggregate),  $\mu_1^o$  is the chemical potential of a single amphiphile in dilute solution, T is the temperature of the system, and R is the universal gas constant.  $\Delta \mu_{aggr}$  depends on both the aggregate shape and N.

 $\Delta\mu_{aggr}$  was calculated using the thermodynamic cycle shown in Figure 2.  $\mu_N^o$  is equal to the free energy change for inserting an AHL into an aggregate,  $\Delta G_{0\to agg}$ , and  $\mu_1^o$  is equal to the hydration free energy of an AHL,  $\Delta G_{0\to w}$ . These free energies were obtained from alchemical free energy calculations and  $\Delta\mu_{aggr}$  was then computed from their difference according to Equation 3:

$$\Delta\mu_{aggr} = -(\mu_1^o - \mu_N^o) = -(\Delta G_{0\to w} - \Delta G_{0\to agg}) \tag{3}$$

 $\Delta G_{0 \to w}$  was calculated by modifying the potential energy function of the system using two coupling parameters,  $\lambda_{elec}$  and  $\lambda_{vdw}$ , which scale the electrostatic and van der Waals interactions of the AHL with the rest of the system. Coupling parameters were varied from zero, corresponding to an AHL in solution, to one, corresponding to an AHL in the gas phase that does not interact with the rest of the system, in 21 independent simulations. The corresponding free energy change for this transformation was computed using the Multistate Bennett Acceptance Ratio (MBAR) method.  $^{35}$   $\Delta G_{0 \to agg}$  was similarly calculated in 27 independent simulations using three coupling parameters,  $\lambda_{elec}$ ,  $\lambda_{vdw}$  and  $\lambda_{rest}$ , with  $\lambda_{rest}$  scaling the value of a harmonic restraint that was applied to ensure the AHL molecule remained in the aggregate as interactions with the system were modified. Complete details on all alchemical free energy calculations are provided in the Supporting Information.

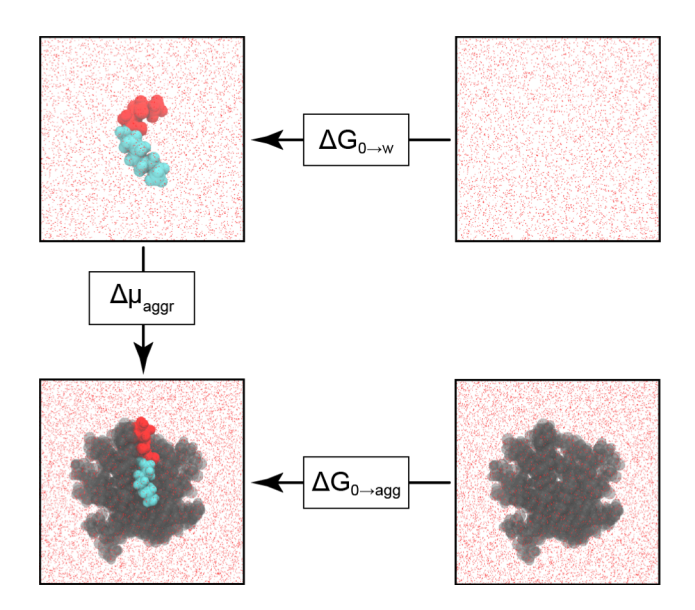


**Figure 2:** Thermodynamic cycle for calculating the free energy change for aggregation,  $\Delta\mu_{aggr}$ , for a representative AHL (3-oxo-C12-AHL). The head and tail groups of the AHL are drawn in red and cyan, respectively. The free energy change upon removing the AHL from the system was calculated by setting the coupling parameters to zero. The remaining AHLs in the aggregate are drawn in gray. Water is shown as red points.

#### **Results and Discussion**

Experimental Characterization of the Critical Aggregation Concentrations of AHLs

Davis *et al.* previously used static light scattering to characterize the aggregation behavior of AHLs in a sucrose buffer containing 0.5% DMSO (v/v) to aid in AHL solubility (whereas short-tailed AHLs are readily soluble in aqueous solution, longer-tailed AHLs can be difficult to dissolve in water).<sup>22</sup> Those past studies suggested that AHLs with more than 12 carbons in the alkyl tail form aggregates in solution, with reported CACs of 4 μM, 17 μM, and 247 μM for C12-AHL, 3-oxo-C14-AHL, and 3-oxo-C12-AHL, respectively. In contrast, AHLs with alkyl tails shorter than 12 carbons were not reported to aggregate at concentrations below 400 μM under these conditions. We performed a series of initial experiments using solutions of 3-oxo-C12-AHL prepared using the sucrose buffer reported by Davis *et al.* and 0.5% DMSO

(v/v). Under these conditions, we observed the rapid formation of large, visible white precipitates at high concentrations that frustrated meaningful characterization of the CAC by light scattering and necessitated the selection of an alternate medium for analysis. In all studies described below, we used solutions of AHLs prepared using either deionized water or LB medium (a common bacterial growth medium) containing 1% DMSO (v/v), unless otherwise noted. These conditions eliminated the formation of large visible precipitates and led to consistent and reproducible results in all of the experiments described below. Aqueous buffer and LB medium containing 1% DMSO (v/v) have been used in past studies to investigate natural and synthetic AHLs in bacterial cultures. Beginning 194. These conditions were thus also adopted here to permit potential future connections between the results of this physicochemical study and those past microbiological studies.

We used both static light scattering and surface tension measurements to characterize the aggregation behaviors of AHLs as a function of AHL concentration. These measurements are complementary and, thus, allowed us to characterize and confirm the formation of aggregated structures in solution using two different methods. Representative results arising from these two methods to characterize the CAC of 3-oxo-C12-AHL are shown in Figure 3 and are discussed in greater detail below.

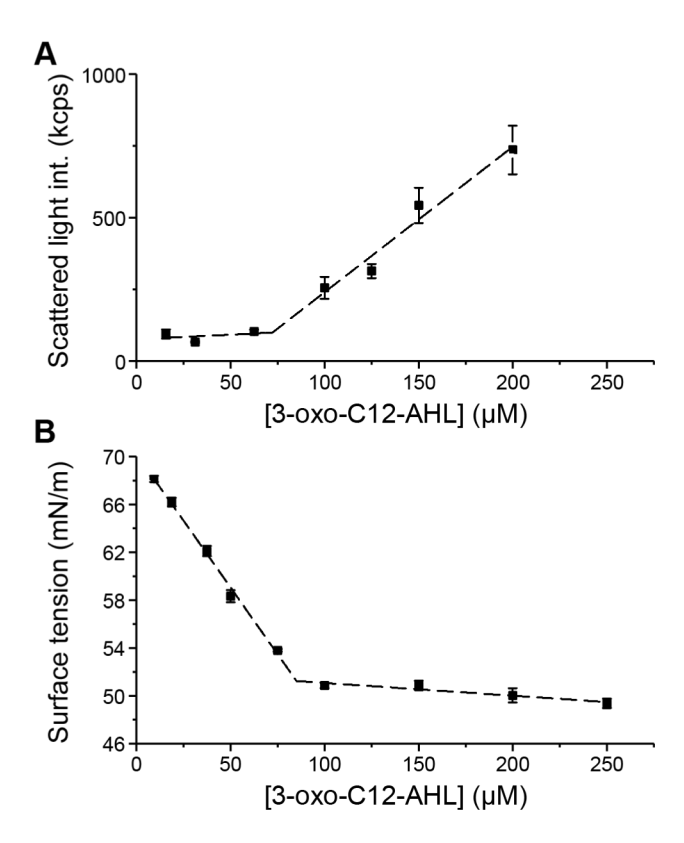


**Figure 3:** Representative plots illustrating the calculation of the CAC for 3-oxo-C12-AHL using (A) light scattering at 30 °C, and (B) surface tension measurements. Error bars represent the standard deviation of three measurements for a single sample. The dashed lines represent the linear regression in (A) and (B). The CAC is calculated as the AHL concentration at which the two regression lines intersect. CACs reported in the main text (Table 1) are the average of three independent samples. Data for all samples are presented in the Supporting Information.

We first characterized the CACs of C4-AHL and 3-oxo-C12-AHL, which again are the two native AHLs used to regulate QS in *P. aeruginosa*. Solutions of 3-oxo-C12-AHL in deionized water at 30 °C exhibited characteristic signs of aggregation corresponding to a CAC of 88 μM (Table 1; data sets from which CACs were extracted are included in the Supporting Information). These results are, in general, consistent with those reported by Davis *et al.*, although the CAC we report here (88 μM) is three-fold lower than the value reported in that past study (247 μM). This disparity is likely a result, at least in part, of differences in the solution conditions used here (we note further that, in our hands, 3-oxo-C12-AHL begins to visibly

precipitate in both sucrose buffer and water at a concentration of ~250  $\mu$ M). The CAC measured here for 3-oxo-C12-AHL using light scattering (88  $\mu$ M) was also similar to the CAC determined using surface tensiometry (97  $\mu$ M, see Table 1). In contrast, while solutions of C4-AHL did show increased scattered light intensity at increasing concentrations of C4-AHL, they did not exhibit decreasing surface tension at increasing concentrations. The lack of surface activity associated with this short-tailed AHL is not consistent with processes of cooperative self-assembly typical of other amphiphilic molecules; the observation of scattered light intensity at increasing concentration in the absence of surface activity suggests that C4-AHL may behave more like a hydrotrope in aqueous solution.<sup>36</sup>

**Table 1:** Experimentally measured CACs of naturally occurring AHLs.

	CACs (μM)		
AHL	Light scattering		Surface tension
	Water <sup>a</sup>	LB medium <sup>b</sup>	Water <sup>c</sup>
C4-AHL	No aggregation		
3-oxo-C8-AHL	$1920 \pm 150$	$2020\pm20$	$2170 \pm 250$
3-oxo-C12-AHL	$88 \pm 20$	$78 \pm 17$	$97 \pm 11$
C12-AHL	$3.7 \pm 0.3$	$3.8 \pm 0.4$	$4.0\pm0.2$
C16 AHL	$0.12 \pm 0.14$	$0.09 \pm 0.02$	$0.16 \pm 0.04^{**}$

Experiments performed at <sup>a</sup>30 °C in deionized water, <sup>b</sup>37 °C in LB medium, and <sup>c</sup>room temperature (RT) in deionized water. All experiments contained 1% DMSO in the aqueous phase. The CAC values reported are the averages and standard deviations of three replicates. \*\*See SI (Figure S1B) for further discussion.

We next characterized the CACs of four additional native AHLs (C6-AHL, 3-oxo-C8-AHL, C12-AHL, and C16-AHL; Figure 1) using light scattering and surface tension measurements. The three longer-chained AHLs (*i.e.*, 3-oxo-C8-AHL, C12-AHL and C16-AHL)

exhibited characteristic signs of aggregation in both measurements, with CACs of 1920 μM, 3.7 μM, and 120 nM, respectively, in the light scattering measurements (Table 1; data from which these results were extracted are included in the Supporting Information). Similar to the results for 3-oxo-C12-AHL, CACs determined by the surface tension measurements were in reasonable agreement with the CACs determined by static light scattering. We note that the concentrations of AHLs in solution and their corresponding changes in surface tension were small when compared to changes in surface tension observed for other common surfactants characterized using this surface tension measurements (see the Supporting Information for further discussion of light scattering and surface tension results).<sup>37-39</sup> We therefore used linear regressions of surface tension against concentration, rather than logarithmic plots, to fit these data and obtain secondary measurements of the CAC.

In contrast to the longer-chained AHLs, for solutions of C6-AHL, linear regression of the scattered light intensity at increasing AHL concentrations resulted in negative values of CAC in several samples, and none were comparable to the concentrations at which surface tension was observed to become constant. As a result, we were unable to conclude whether assemblies formed in solutions of C6-AHL were likely to result from cooperative self-assembly. Further discussion of the behavior exhibited by C4-AHL and C6-AHL in these two measurements is provided in the Supporting Information.

Overall, we observed CACs to decrease as AHL tail length increased (Table 1). This behavior is similar to that of other families of cationic, anionic, and nonionic surfactants in aqueous solution. The molecular structure of the AHL head group also had a significant impact on CAC; the addition of a single 3-oxo group to C12-AHL (to form 3-oxo-C12-AHL), resulted in an order of magnitude increase in the CAC from 3.7 µM to 88 µM (Table 1). This

observation is generally consistent with results reported by Davis *et al.*, using these two AHLs.<sup>22</sup> In contrast with Davis *et al.* however, we observed that the shorter chained 3-oxo-C8-AHL did aggregate in solution.

We performed a second set of light scattering measurements to characterize AHL CACs in LB medium at 37 °C, a set of environmental conditions used in past microbiological studies of these compounds.<sup>8-9, 12, 14</sup> Table 1 shows that the changes in ionic strength and temperature did not impact the CACs of these AHLs compared to those in water at room temperature. In addition, to determine if the presence of additional DMSO in solution impacted the CACs of the AHLs studied, static light scattering measurements were performed on a solution of C12-AHL in water containing 1.5% DMSO. The CAC of C12-AHL measured under these conditions was 6.6 μM (data not shown), suggesting that the additional DMSO does not have a significant impact on the formation of aggregates. Finally, we characterized the zeta potentials of aggregates of these AHLs using solutions of 3-oxo-C12-AHL, C12-AHL, and C16-AHL at concentrations above their measured CACs in water at 30 °C. The aggregates in these solutions exhibited negative zeta potentials with magnitudes ranging from -20 mV to -44 mV (see Figure S3). When combined, these results support the view that non-ionic AHLs can engage in cooperative self-assembly and provide insight into structural features that can govern this behavior. We return to a discussion of additional physical characterization of these aggregates by transmission electron microscopy (TEM) and dynamic light scattering (DLS) in the sections below.

# Unbiased Molecular Dynamics Simulations of AHL Aggregation

The experimental characterization methods used above do not provide information about the sizes, shapes, or morphologies of the AHL aggregates that form at or above CAC. To obtain

molecular-scale insight into factors that could influence AHL self-assembly and resulting selfassembled structures, we performed 50-ns unbiased atomistic MD simulations of C4-AHL molecules and 3-oxo-C12-AHL molecules in water. Figure 4A-B shows the atomistic representation of these molecules. We first performed simulations of either 64 C4-AHL or 3oxo-C12-AHL molecules initialized in well-separated positions in water. This number of molecules is similar to the typical aggregation number (i.e., number of molecules per aggregate) for many nonionic surfactants. 40-42 Figure 4A shows that C4-AHL molecules remain dispersed at the end of the simulation. Conversely, Figure 4B shows that 3-oxo-C12-AHL molecules rapidly self-assemble within the same simulation timescale to form a spherical micelle. These results are generally consistent with our experimental measurements, in which 3-oxo-C12-AHL exhibited characteristic signs of aggregation, but we were unable to clearly interpret the behavior of C4-AHL. We next performed additional unbiased MD simulations of 3-oxo-C12-AHL self-assembly with a larger number of molecules to determine whether non-spherical structures with larger aggregation numbers could also form. Rather than form multiple smaller micelles, Figure 4C shows that simulations of 216 3-oxo-C12-AHL molecules self-assemble into a cylindrical aggregate. Furthermore, Figure 4D shows that collections of 512 3-oxo-C12-AHL molecules self-assemble into a bilayer-like structure. These results suggest that AHLs can form extended aggregates that would have much larger sizes than conventional micelles. However, the actual concentration of AHLs in these simulations is much higher than values used in the experiments above; thus, these simulations can only qualitatively confirm and predict self-assembly trends in agreement with related experimental observations (see further discussion below).

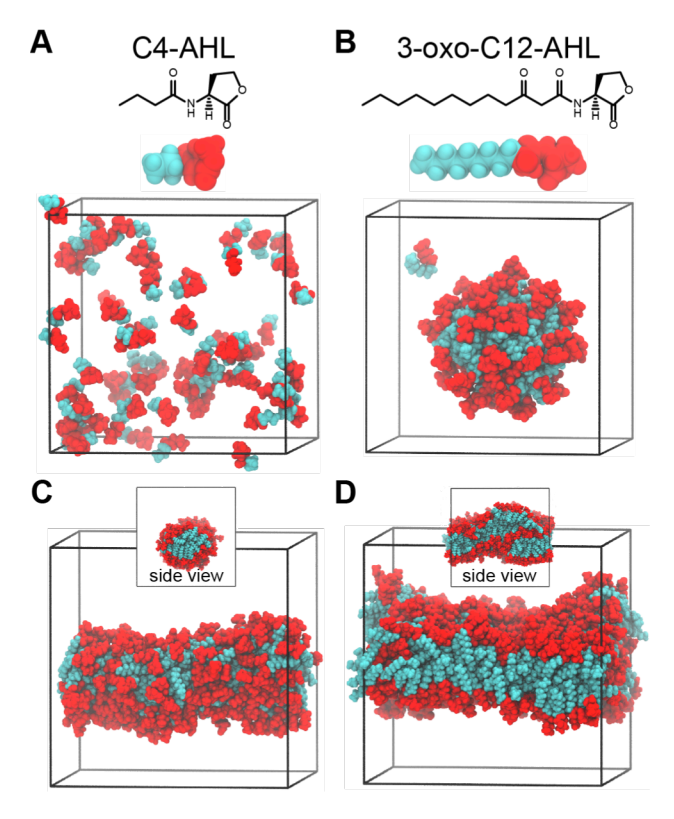


**Figure 4:** Simulation snapshots from 50-ns unbiased MD simulations. All snapshots are of final simulation configurations. Water molecules are not shown for clarity. AHL head groups are red and tail groups are cyan. (A) Simulation of 64 C4-AHL molecules in water, which remain dispersed within the simulation timescale. The structure of C4-AHL and corresponding atomistic MD representation are shown at top. (B) Self-assembly of 64 3-oxo-C12-AHL molecules in water to form a spherical micelle. The structure of 3-oxo-C12-AHL and corresponding atomistic MD representation are shown at top. (C-D) Self-assembly of 216 and 512 3-oxo-C12-AHL molecules to form (C) a cylindrical aggregate and (D) a bilayer-like structure. The insets show side views of the aggregates.

# Free Energy Calculations for the Determination of Self-Assembled Structures

The CACs of AHLs cannot be directly determined using the unbiased simulations because experimentally relevant aggregation numbers and AHL concentrations cannot be modeled at atomistic resolution. To complement the unbiased simulations and provide additional insight into trends observed in our experimental CAC results, we calculated  $\Delta\mu_{aggr}$  using alchemical free energy calculations to compare self-assembly thermodynamics between

simulations and experiments. In general, the aggregation free energy depends on both aggregate structure and the aggregation number.<sup>34</sup> We thus hypothesized that the structure that minimizes  $\Delta\mu_{aggr}$  for a given AHL corresponds to the equilibrium structure formed by that AHL in solution. We computed  $\Delta\mu_{aggr}$  for AHLs assembled into spheres, cylinders, and bilayers to correspond to the three limiting structures identified in the unbiased simulations. These calculations allowed us to test the hypothesis that cylindrical or bilayer structures could be lower free energy structures than spherical micelles for some AHLs, corresponding to the possible formation of extended aggregates in solution. For each AHL, we also modeled three spherical aggregates with different aggregation numbers (N = 20, 50, and 100). Known aggregation numbers for single-tailed surfactants are generally in this range. 40-43 Moreover these aggregation numbers produce roughly spherical micelles based on the calculation of the asphericity of the resulting aggregates (as described in the Supporting Information), a parameter that has been used previously to validate the aggregation number for spherical micelles.<sup>43</sup> The aggregation numbers for the cylindrical aggregates and bilayers was effectively infinite because both structures spanned the periodic boundaries of the simulation boxes. We thus ignored potential end effects associated with these structures, although in an experimental system any self-assembled bilayer structure that formed in solution would likely lead to the formation of vesicles to eliminate end effects. Similarly, we also neglected the effect of vesicle curvature, which would introduce an additional elastic free energy term not considered in the alchemical free energy calculation. Simulations of 1-palmitoyl-2-oleoyl-glycero-3-phosphocholine (POPC) were performed as a control to validate our methodology; as expected,  $\Delta\mu_{aggr}$  was lowest for a bilayer structure (see Supporting Information, section S8), which agrees with the experimental observation that lipids self-assemble into vesicles.

 $\Delta\mu_{aggr}$  was only calculated for starting structures that remained stable during initial equilibration. All C4-AHL, C6-AHL, and 3-oxo-C8-AHL systems dispersed during equilibration, indicating that none of these AHLs formed stable aggregates in the simulations. These AHLs were excluded from the  $\Delta\mu_{aggr}$  calculations. We note, however, that 3-oxo-C8-AHL was observed to form aggregates in the experiments described above, which contradicts the simulation results; this discrepancy could result from small systematic error in the simulation force field parameterization, as discussed further below. Starting structures generated for C8-AHL and 3-oxo-C10-AHL bilayers formed a slab of AHLs with no defined structure at the end of the equilibration, instead of a defined bilayer structure with the head groups arranged at the periphery of the aggregate and tail groups forming the core of the bilayer. We interpret this result to indicate that C8-AHL and 3-oxo-C10-AHL do not form stable bilayers and thus excluded these systems from the  $\Delta\mu_{aggr}$  calculations.

Figure 5 reports values of  $\Delta\mu_{aggr}$  for spherical micelles formed from 3-oxo-C12-AHL, C12-AHL, and C16-AHL calculated from simulations. Figure 5 also shows values of  $\Delta\mu_{aggr}$  determined from our experimentally measured CACs using light scattering at 37 °C in LB medium using Equation 2, which can be compared to the simulation values to validate the modeling approach. We expected agreement for spherical micelles because they have smaller aggregation numbers than larger aggregates (*e.g.*, vesicles), which often require the input of external energy (*e.g.*, by sonication) to overcome kinetic barriers for spontaneous formation. Simulation calculations of  $\Delta\mu_{aggr}$  are reported for all three aggregation numbers because the preferred aggregation number of spherical micelles formed experimentally is unknown; thus, we anticipate that the aggregation number corresponding to the simulation value of  $\Delta\mu_{aggr}$  that most closely matches the experimentally determined value would correspond to the experimentally

observed micelle size. Both the simulation and experimental values of  $\Delta\mu_{aggr}$  exhibit similar trends: increasing the aliphatic tail length decreases  $\Delta\mu_{aggr}$  (indicating more favorable aggregation) while adding a 3-oxo group to C12-AHL increased  $\Delta\mu_{aggr}$ . The closest agreement between the simulated and experimentally determined values of  $\Delta\mu_{aggr}$  was found for the largest spherical micelles studied (N=100), suggesting that these micelles are thermodynamically preferred. This observation is consistent with prior studies of nonionic amphiphiles which exhibit aggregation numbers between 80-150. The MD simulations do systematically underestimate the magnitude of  $\Delta\mu_{aggr}$  compared to the experimental measurements, which may result from errors associated with force fields or underestimated aggregation numbers. Nonetheless, these results demonstrate that our simulation methodology can predict qualitative trends for AHL self-assembly that agree with experimental observations, permitting further interrogation of self-assembly thermodynamics, and suggest that AHL micelles form with ~100 molecules per aggregate.

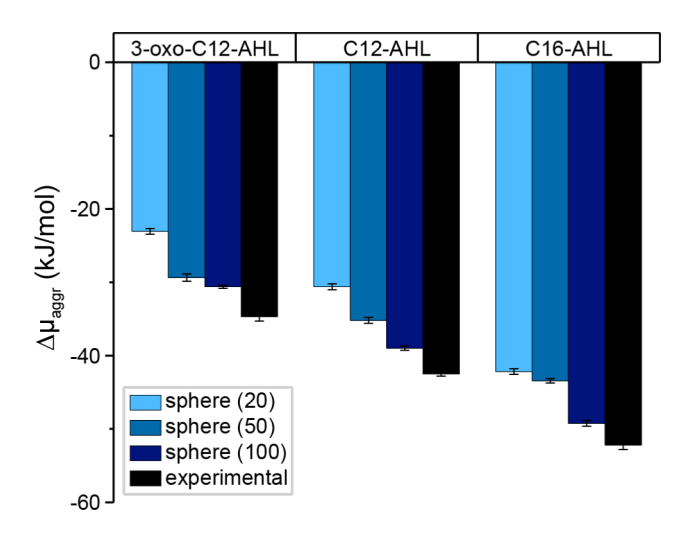


**Figure 5:** Comparison of  $\Delta\mu_{aggr}$  using experimentally calculated CACs obtained by light scattering at 37 °C in LB medium to  $\Delta\mu_{aggr}$  calculated using alchemical free energy calculations. The experimental error bars represent standard error and simulation error bars represent standard deviation.

We next sought to determine if extended aggregates could be more thermodynamically favorable than spherical micelles for some AHLs. Figure 6 and Table S2 of the Supporting Information show plots of  $\Delta\mu_{aggr}$  for AHLs shown in Figure 1 (including AHL structures that were not characterized experimentally in the studies described above) as a function of tail length and the absence (Figure 6A) or presence (Figure 6B) of a 3-oxo group in the head group.  $\Delta\mu_{aggr}$  is reported for all three spherical structures (N=20, 50, and 100) as well as extended cylindrical and bilayer aggregates. In these plots, the lowest value of  $\Delta\mu_{aggr}$  for any given AHL indicates the most thermodynamically preferred structure predicted for that compound. As the AHL tail length increases, extended aggregates (cylindrical aggregates and bilayers) are increasingly preferred compared to spherical micelles. In particular, the simulations predict that C14-AHL, C16-AHL, and 3-oxo-C16-AHL strongly prefer bilayer formation and that 3-oxo-C14-AHL should exhibit a similar thermodynamic preference for both extended cylinders and bilayers. These results are generally consistent with trends based on the molecular packing parameter, as

increasing the AHL tail length would increase the packing parameter to prefer increasingly planar structures consistent with extended aggregates.<sup>34</sup> These findings predict that, irrespective of the relatively small difference in the structures of their head groups, long-tailed C14- and C16-AHLs should self-assemble into vesicle-like structures at equilibrium. Our simulation results suggest that all other AHLs studied here (C8-, C10- and C12- AHLs) should prefer to form medium- to large-sized spherical aggregates containing 50 to 100 molecules, although we note that there is only a small difference between values of  $\Delta\mu_{aggr}$  for spherical and extended aggregate structures for these AHLs.

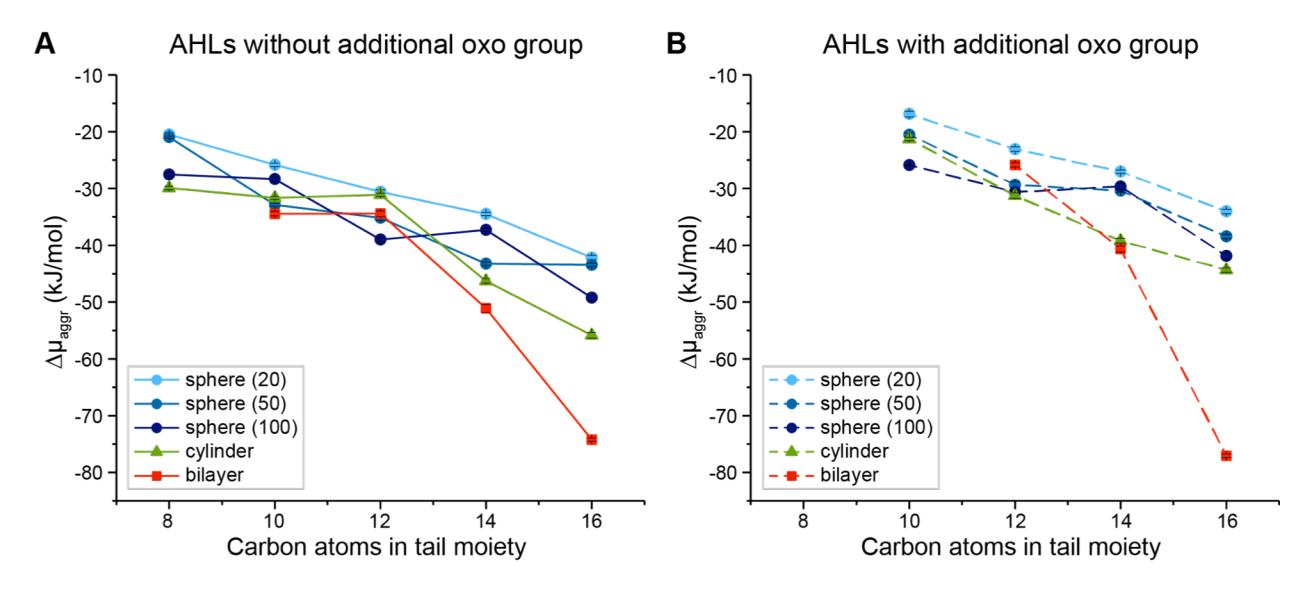


**Figure 6:**  $\Delta\mu_{aggr}$  for each AHL structure in kJ/mol. The solid and dashed lines represent AHLs without and with the oxo additional group in the head moiety, respectively. Error bars represent the standard deviation and are generally smaller than the symbols.

# Experimental Characterization of Aggregate Size and Morphology

We used TEM to characterize the sizes and structures of aggregates formed in solutions of AHLs and determine whether key outcomes predicted by our MD simulations could be observed experimentally. In a first series of studies, we characterized aggregates formed in

solutions of 3-oxo-C12-AHL and C12-AHL because our simulations predicted no strong thermodynamic bias for the formation of micelles or bilayer structures for these compounds. All imaging experiments were performed using solutions of AHLs at concentrations above their experimentally determined CACs (Table 1) in water at ambient room temperature, and samples were stained with a 2% uranyl acetate solution prior to imaging using a procedure reported in past studies to characterize surfactant self-assembly. Panels A-D of Figure 7 show representative TEM images of aggregates formed by 3-oxo-C12-AHL (A-B) and C12-AHL (C-D) and reveal evidence of nanoscale structures in both samples. In general, these nanostructures and all others described below were spherical or quasi-spherical in shape, and they appeared to be singular particulate structures. We did not observe particle clustering, evidence of flocculation, or 'aggregates of aggregates', consistent with the observation of large and negative zeta potentials measured for solutions of these AHLs and the colloidal stability that that would impart (as described above; see Figure S3).

Further inspection of these images reveals these samples to be comprised of distributions of aggregates with substantially different sizes. Analysis of aggregate sizes using Image J revealed samples of 3-oxo-C12-AHL to contain both smaller aggregates with average diameters of  $6.8 \pm 1.7$  nm and larger aggregates with average diameters of  $36.4 \pm 7.2$  nm (histograms showing the results of these analyses are provided in Figure S9 of the Supporting Information). Analysis of samples of C12-AHL also revealed populations of both smaller and larger aggregates, with average diameters of  $7.1 \pm 1.8$  nm and  $22.1 \pm 9.7$  nm, respectively. In some samples of C12-AHL, we also occasionally observed the existence of a small number of substantially larger aggregates around ~50-200 nm in diameter (Figure S12); however, the vast majority of particles observed in these samples had average sizes on the order of 30 nm or below.

The average sizes of the smaller aggregates in samples of 3-oxo-C12-AHL and C12-AHL are similar to the sizes of the 100-molecule spherical aggregates predicted by our MD simulations (diameters were calculated to be ~6.1 nm and ~6.4 nm for 3-oxo-C12-AHL and C12-AHL, respectively; see Supporting Information for additional details of these calculations).

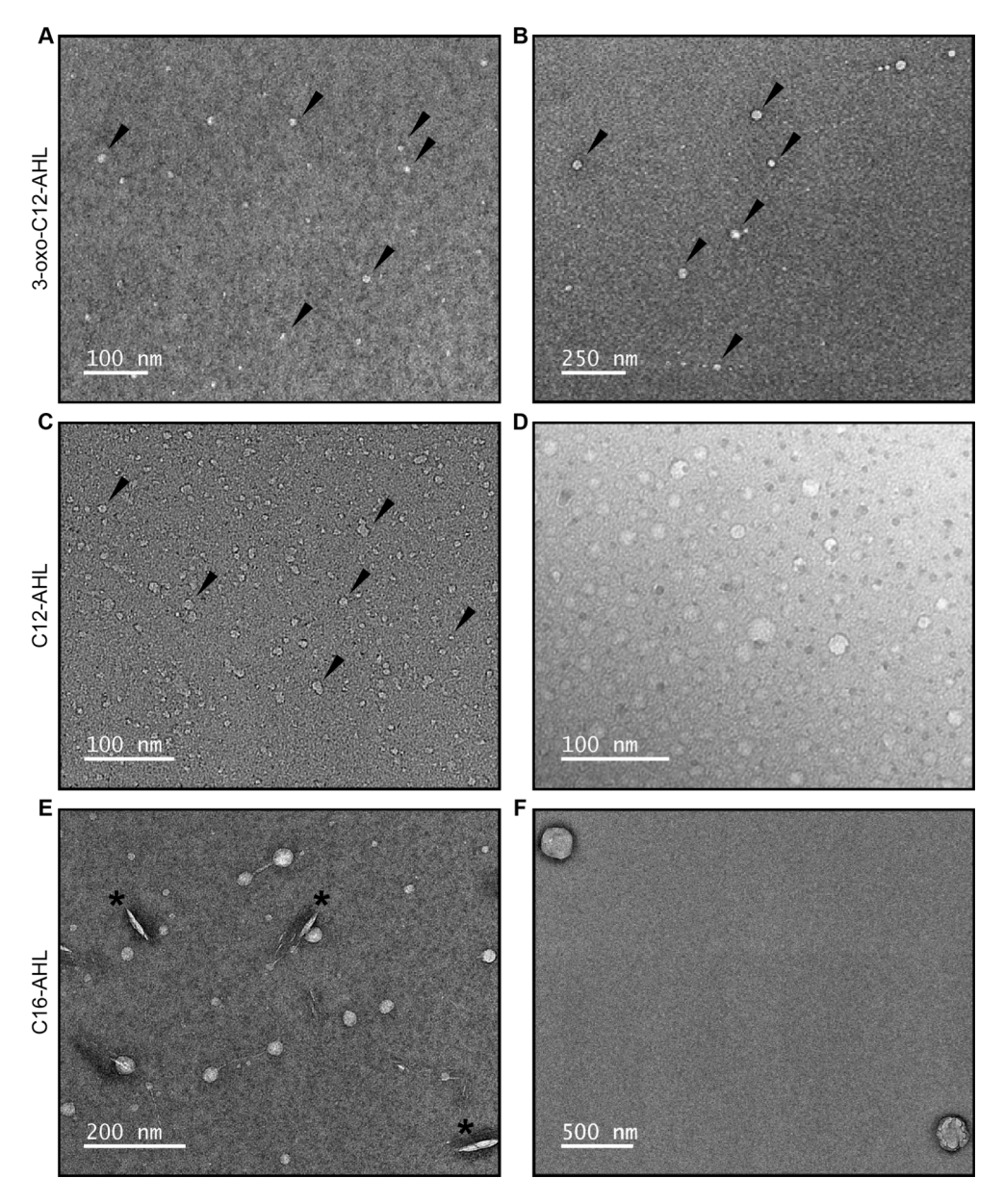


**Figure 7:** TEM images of samples of (A,B) 3-oxo-C12-AHL, (C,D) C12-AHL, and (E,F) C16-AHL in water. The black arrows in (A-C) identify representative examples of aggregates in these samples and the black asterisks in (E) identify defects arising from the staining of that sample.

These values are also consistent with sizes typically associated with micelles formed by conventional small-molecule amphiphiles. The sizes of the larger aggregates in these samples are larger than those reported for conventional micelles and are consistent with the presence of extended bilayer structures (for example, small unilamellar vesicles of phospholipids often form in a size range of 20-100 nm). In general, these results are consistent with predictions arising from Figure 6, which predicts the aggregation free energies for spherical aggregates and extended cylindrical/bilayer structures to be similar for both C12-AHL and 3-oxo-C12-AHL, indicating that both types of aggregate structures may form in solution. We note, however, that our simulations did not consider the formation of alternative structures that could also fall within a similar size range, such as discoidal aggregates or multilayer structures. Our simulations also neglect the elastic free energy associated with forming small vesicles that could modify the size distribution.

We also imaged samples prepared from solutions of C16-AHL, as the simulations above predicted that this compound should strongly prefer the formation of bilayer structures (Figure 6). The images shown in Figure 7E-F are generally consistent with that prediction. These images show aggregates with average sizes that are substantially larger than those shown in Figure 7A-D, with average diameters of  $28.6 \pm 7.2$  nm (Figure 7E) and some structures as large as 250 nm (Figure 7F). We note that closer inspection of the image in Figure 7E also reveals some aggregates to be connected by long, thin tubular structures. The origin of these tubular structures is not clear, and we caution that they could be artifacts arising from shear experienced by these aggregates during the staining and preparation of these samples for analysis. These observations are interesting, however, because they also hint at the possibility that these vesicular AHL aggregates could be capable of undergoing further transformations or exhibiting

other dynamic behaviors similar to those observed in other phospholipid vesicles or other self-assembled vesicle systems. 49-51

Overall, the results of these TEM experiments are consistent with the results of our MD simulations, which predicted a transition from the formation of spherical micelles to the formation of more extended bilayer structures upon progression from C12-AHL to C16-AHL. In a subsequent series of imaging experiments, we used TEM to characterize solutions of 3-oxo-C8-AHL as a representative shorter-tailed AHL that was observed experimentally to form aggregates (Table 1) but was not predicted to form stable aggregates in our simulations. The results of those experiments are shown in Figure S11. In general, these samples consisted of larger aggregates with average diameters of ~60 nm, consistent with the formation of vesicular structures. We did not observe smaller aggregated structures similar to those shown in Figure 7A-D formed in solutions of C12-AHL and 3-oxo-C12-AHL. The factors influencing the apparent anomalous behavior of this shorter-tailed AHL are not currently understood.

The results of our TEM experiments reveal solutions of AHLs to contain aggregates with sizes that are generally consistent with those predicted by our MD simulations. We note, however, that negative stain TEM is inherently limited to characterization of relatively small numbers of particles. This method can also potentially introduce artifacts resulting from the dynamic reorganization of self-assembled structures during the staining/dehydration process. We therefore performed a final series of characterization experiments using DLS to provide additional information about the sizes of larger populations of hydrated aggregates suspended in aqueous solution. All DLS measurements reported here were prepared at 30 °C using solutions of AHLs in water at concentrations above their previously determined CACs; no particles of discernable size were observed at sub-CAC concentrations of AHL under these conditions.

Autocorrelation functions and corresponding calculated particle size distributions for all measurements discussed below are provided in Figure S10 of the Supporting Information.

Characterization of solutions of C16-AHL by DLS yielded number and intensity average size distributions with a single peak corresponding to particles with an average hydrodynamic diameter of ~100 nm. This value is consistent with the presence of larger vesicular structures and on the order of the sizes of aggregates observed for this AHL by TEM (Figure 7E-F), suggesting that the larger structures identified in Figure 7E-F were not the result of artifacts introduced during the staining of those samples. Characterization of solutions of C12-AHL also yielded unimodal number and intensity average size distributions corresponding to particles with average hydrodynamic diameters of ~350 nm. This average size is substantially larger than the sizes of particles observed by TEM for C12-AHL (Figure 7C-D), and our DLS results did not reveal evidence of a population of smaller aggregates (as observed by TEM; Figure 7C-D and Figures S12). As noted above, we did observe a small number of larger (~50-200 nm) aggregates in solutions of C12-AHL by TEM (Figure S12). It is possible that the presence of those larger particles, which would scatter substantially more light than a smaller particle, could obscure the presence of any micellar-sized aggregates that may be present in those samples. Such behavior has been observed previously for the DLS characterization of mixtures of nanoparticles having substantially different sizes, where often only the larger population of particles may be observed. 52-55 We note, in this context, that we did obtain autocorrelation functions that were consistent with a more complex distribution of particle sizes in solutions of 3-oxo-C12-AHL (Figure S10). However, solutions of this AHL proved difficult to characterize with run-to-run consistency. Multiple non-linear least squares algorithms including CONTIN analyses of those samples returned bimodal size distributions (Figure S10), which is consistent with the

observation of both small and large populations of aggregates in samples of this AHL by TEM. However, we were not able to obtain fits to the scattering functions that were sufficient to report meaningful size distributions for solutions of this AHL.

Finally, we note that Davis *et al.* previously reported the use of DLS to characterize solutions of 3-oxo-C14-AHL in aqueous buffer. That study reported the average hydrodynamic diameter of aggregates of that AHL to be ~22 nm and interpreted that result to suggest that 3-oxo-C14-AHL can self-organize into micelles. We did not characterize solutions of 3-oxo-C14-AHL experimentally as part of this current study. We comment, however, that 22 nm is substantially larger than the size expected for a conventional spherical micelle, and that aggregates of that approximate size are consistent with those of the larger vesicular aggregates observed in our TEM images of solutions of 3-oxo-C12-AHL and C12-AHL. We thus consider it possible that solutions of 3-oxo-C14-AHL, as characterized in that prior study, could also form larger vesicular structures. This possibility is further supported by the results of our MD simulations, which predict that the formation of cylinders or bilayer structures should be more thermodynamically favorable for 3-oxo-C14-AHL than the formation of spherical micelles (Figure 6).

# **Summary and Conclusions**

In this work, we combined biophysical characterization techniques, electron microscopy, and MD simulations to investigate the self-assembly of 12 AHLs representative of the lipophilic signal class used by Gram-negative bacteria for quorum sensing (QS). We used static light scattering and surface tension measurements to determine that 3-oxo-C8-AHL, 3-oxo-C12-AHL, C12-AHL, and C16-AHL self-assemble in aqueous solution and to characterize their

corresponding CACs. In general, CACs decreased with increasing tail length. The CAC for 3oxo-C12-AHL was an order of magnitude higher than that of C12-AHL, revealing the impact of AHL head group chemistry on self-assembly. Atomistic MD simulations predicted that 3-oxo-C12-AHL molecules self-assemble in unbiased simulations into spherical, cylindrical, or bilayerlike aggregates. We then utilized alchemical free energy calculations to determine thermodynamically preferred aggregate structures. These calculations determined that AHLs with 10 or 12 tail carbon atoms likely form spherical micelles containing approximately 100 molecules, while AHLs with 14 or 16 tail carbon atoms are likely to form vesicles in solution. DLS measurements and TEM images both confirmed the existence of aggregates in solution with sizes consistent with spherical micelles or small unilamellar vesicles for 3-oxo-C12-AHL and C12-AHL. In addition, the TEM images revealed the formation of large vesicles (~250 nm) in aqueous solutions of C16-AHL. These experimental findings are in general agreement with our simulation predictions. When combined, our results provide new physical insight into the aggregation behavior of AHLs in aqueous solution and further demonstrate the ability of atomistic MD simulations to quantify the thermodynamic preference of various aggregate morphologies.

In closing, we note that our results also raise several interesting questions regarding the potential biological relevance of AHL aggregation. Notably, the experimentally determined CAC of C16-AHL observed here (0.12 μM) is lower than the concentration reported to be present in some bacterial supernatants (5 μM),<sup>18</sup> suggesting that the vesicle-like aggregates observed here for C16-AHL could also potentially form in the presence of bacterial communities. We also recently reported the concentration of 3-oxo-C12-AHL in cultures of *P. aeruginosa* at low micromolar levels,<sup>56</sup> suggesting the possibility that this AHL (with a CAC of 88 μM) could also

rise to concentrations needed form aggregates in cultures of this organism. We also note that AHLs can be present at substantially higher concentrations within bacterial biofilms (e.g., as high as ~630 μM),<sup>57</sup> and there is a concentration gradient of AHLs in the vicinity of cells where local concentrations may be sufficiently high to promote aggregation.<sup>58-59</sup> It is therefore possible that AHLs could form aggregates in biologically relevant environments, and that those aggregates could play roles in mediating the transport of AHLs between cells or within biofilms. It is, of course, also likely that aggregate structures containing AHLs could be formed by coassembly of AHLs with other natural amphiphiles, such as phospholipids or other biosurfactants produced under the control of QS (e.g., the rhamnolipids produced by P. aeruginosa).<sup>60</sup> Elucidating the potential biological impacts of AHL self-assembly and the potential for coassembly with other biological or synthetic amphiphiles will require additional study. The results of this current work, however, provide the first necessary steps toward building a more rigorous understanding of QS signaling molecular transport mechanisms.

Acknowledgments. Financial support for this work was provided by the National Science Foundation through a grant provided to the UW-Madison Materials Research Science and Engineering Center (MRSEC; DMR-1720415). The authors acknowledge the use of instrumentation supported by the NSF through the UW MRSEC (DMR-1720415). C.G.G. was supported in part by a NSF Graduate Research Fellowship. K.E.N. was supported in part by the UW-Madison NIH Chemistry–Biology Interface Training Program (T32 GM008505), and the UW-Madison Office of the Vice Chancellor for Research and Graduate Education (with funding from the Wisconsin Alumni Research Foundation). The authors gratefully acknowledge Desirée

Benefield for many helpful discussions and assistance with training and the acquisition and analysis of TEM images.

# References

- 1. Miller, M. B.; Bassler, B. L. Quorum Sensing in Bacteria. *Annu. Rev. Microbiol.* **2001,** *55*, 165-199.
- 2. Waters, C. M.; Bassler, B. L. Quorum Sensing: Cell-to-Cell Communication in Bacteria. *Annu. Rev. Cell Dev. Biol.* **2005**, *21*, 319-346.
- 3. Chugani, S. A.; Whiteley, M.; Lee, K. M.; D'Argenio, D.; Manoil, C.; Greenberg, E. P. Qscr, a Modulator of Quorum-Sensing Signal Synthesis and Virulence in Pseudomonas Aeruginosa. *Proc. Natl. Acad. Sci. U. S. A.* **2001,** *98* (5), 2752-2757.
- 4. Papenfort, K.; Bassler, B. L. Quorum Sensing Signal-Response Systems in Gram-Negative Bacteria. *Nat. Rev. Microbiol.* **2016,** *14* (9), 576-588.
- 5. Whiteley, M.; Diggle, S. P.; Greenberg, E. P. Progress in and Promise of Bacterial Quorum Sensing Research. *Nature* **2017**, *551* (7680), 313-320.
- 6. Camilli, A.; Bassler, B. L. Bacterial Small-Molecule Signaling Pathways. *Science* **2006**, *311* (5764), 1113-1116.
- 7. Fuqua, C.; Greenberg, E. P. Listening in on Bacteria: Acyl-Homoserine Lactone Signalling.

  Nat. Rev. Mol. Cell Biol. 2002, 3 (9), 685-695.
- 8. Gerdt, J. P.; McInnis, C. E.; Schell, T. L.; Rossi, F. M.; Blackwell, H. E. Mutational Analysis of the Quorum-Sensing Receptor Lasr Reveals Interactions That Govern Activation and Inhibition by Nonlactone Ligands. *Chem. Biol.* **2014**, *21* (10), 1361-1369.

- 9. Welsh, M. A.; Blackwell, H. E. Chemical Probes of Quorum Sensing: From Compound Development to Biological Discovery. *Fems Microbiol. Rev.* **2016**, *40* (5), 774-794.
- Galloway, W. R. J. D.; Hodgkinson, J. T.; Bovvden, S.; Welch, M.; Spring, D. R. Applications of Small Molecule Activators and Inhibitors of Quorum Sensing in Gram-Negative Bacteria. *Trends Microbiol.* 2012, 20 (9), 449-458.
- Amara, N.; Mashiach, R.; Amar, D.; Krief, P.; Spieser, S. A. H.; Bottomley, M. J.; Aharoni,
   A.; Meijler, M. M. Covalent Inhibition of Bacterial Quorum Sensing. *J. Am. Chem. Soc.* 2009, 131 (30), 10610-10619.
- 12. Moore, J. D.; Rossi, F. M.; Welsh, M. A.; Nyffeler, K. E.; Blackwell, H. E. A Comparative Analysis of Synthetic Quorum Sensing Modulators in Pseudomonas Aeruginosa: New Insights into Mechanism, Active Efflux Susceptibility, Phenotypic Response, and Next-Generation Ligand Design. *J. Am. Chem. Soc.* **2015**, *137* (46), 14626-14639.
- 13. O'Reilly, M. C.; Dong, S. H.; Rossi, F. M.; Karlen, K. M.; Kumar, R. S.; Nair, S. K.; Blackwell, H. E. Structural and Biochemical Studies of Non-Native Agonists of the Lasr Quorum-Sensing Receptor Reveal an L3 Loop "out" Conformation for Lasr. *Cell Chem. Biol.* **2018**, *25* (9), 1128-+.
- 14. Boursier, M. E.; Moore, J. D.; Heitman, K. M.; Shepardson-Fungairino, S. P.; Combs, J. B.; Koenig, L. C.; Shin, D.; Brown, E. C.; Nagarajan, R.; Blackwell, H. E. Structure-Function Analyses of the N-Butanoyl L-Homoserine Lactone Quorum-Sensing Signal Define Features Critical to Activity in Rhir. Acs Chem. Biol. 2018, 13 (9), 2655-2662.
- 15. Kaplan, H. B.; Greenberg, E. P. Diffusion of Autoinducer Is Involved in Regulation of the Vibrio-Fischeri Luminescence System. *J. Bacteriol.* **1985**, *163* (3), 1210-1214.

- Pearson, J. P.; Van Delden, C.; Iglewski, B. H. Active Efflux and Diffusion Are Involved in Transport of Pseudomonas Aeruginosa Cell-to-Cell Signals. *J. Bacteriol.* 1999, 181 (4), 1203-1210.
- 17. Moore, J. D.; Gerdt, J. P.; Eibergen, N. R.; Blackwell, H. E. Active Efflux Influences the Potency of Quorum Sensing Inhibitors in Pseudomonas Aeruginosa. *Chembiochem* **2014**, *15* (3), 435-442.
- 18. Toyofuku, M.; Morinaga, K.; Hashimoto, Y.; Uhl, J.; Shimamura, H.; Inaba, H.; Schmitt-Kopplin, P.; Eberl, L.; Nomura, N. Membrane Vesicle-Mediated Bacterial Communication. *Isme J.* **2017**, *11* (6), 1504-1509.
- 19. Mashburn-Warren, L. M.; Whiteley, M. Special Delivery: Vesicle Trafficking in Prokaryotes. *Mol. Microbiol.* **2006**, *61* (4), 839-846.
- 20. Song, D. K.; Meng, J. C.; Cheng, J.; Fan, Z.; Chen, P. Y.; Ruan, H. F.; Tu, Z. Y.; Kang, N.; Li, N.; Xu, Y., et al. Pseudomonas Aeruginosa Quorum-Sensing Metabolite Induces Host Immune Cell Death through Cell Surface Lipid Domain Dissolution. Nat. Microbiol. 2019, 4 (1), 97-111.
- 21. Daniels, R.; Reynaert, S.; Hoekstra, H.; Verreth, C.; Janssens, J.; Braeken, K.; Fauvart, M.; Beullens, S.; Heusdens, C.; Lambrichts, I., et al. Quorum Signal Molecules as Biosurfactants Affecting Swarming in Rhizobium Etli. Proc. Natl. Acad. Sci. U. S. A. 2006, 103 (40), 14965-14970.
- 22. Davis, B. M.; Richens, J. L.; O'Shea, P. Label-Free Critical Micelle Concentration Determination of Bacterial Quorum Sensing Molecules. *Biophys. J.* **2011**, *101* (1), 245-254.
- 23. Schweighauser, L.; Wegner, H. A. Chemical Talking with Living Systems: Molecular Switches Steer Quorum Sensing in Bacteria. *Chembiochem* **2015**, *16* (12), 1709-1711.

- 24. Hodgkinson, J. T.; Galloway, W.; Casoli, M.; Keane, H.; Su, X. B.; Salmond, G. P. C.; Welch, M.; Spring, D. R. Robust Routes for the Synthesis of N-Acylated-L-Homoserine Lactone (Ahl) Quorum Sensing Molecules with High Levels of Enantiomeric Purity. *Tetrahedron Lett.* 2011, 52 (26), 3291-3294.
- 25. Shinoda, K.; Yamaguchi, T.; Hori, R. The Surface Tension and the Critical Micelle Concentration in Aqueous Solution of Beta-D-Alkyl Glucosides and Their Mixtures. *Bull. Chem. Soc. Jpn.* **1961**, *34* (2), 237-241.
- Gewering, T.; Januliene, D.; Ries, A. B.; Moeller, A. Know Your Detergents: A Case Study on Detergent Background in Negative Stain Electron Microscopy. *J. Struct. Biol.* 2018, 203 (3), 242-246.
- 27. Liu, C. Y.; Wang, Y. Z.; Chai, C. X.; Ullah, S.; Zhang, G. J.; Xu, B. C.; Liu, H. Q.; Zhao, L. Interfacial Activities and Aggregation Behaviors of N-Acyl Amino Acid Surfactants Derived from Vegetable Oils. *Colloids Surf.*, A 2018, 559, 54-59.
- 28. Bajani, D.; Gharai, D.; Dey, J. A Comparison of the Self-Assembly Behaviour of Sodium N-Lauroyl Sarcosinate and Sodium N-Lauroyl Glycinate Surfactants in Aqueous and Aqueo-Organic Media. *J. Colloid Interface Sci.* **2018**, *529*, 314-324.
- Patra, T.; Ghosh, S.; Dey, J. Cationic Vesicles of a Carnitine-Derived Single-Tailed Surfactant: Physicochemical Characterization and Evaluation of in Vitro Gene Transfection Efficiency. *J. Colloid Interface Sci.* 2014, 436, 138-145.
- 30. Jo, S.; Kim, T.; Iyer, V. G.; Im, W. Charmm-Gui: A Web-Based Graphical User Interface for Charmm. *J. Comput. Chem.* **2008**, *29* (11), 1859-65.

- 31. Kim, S.; Lee, J.; Jo, S.; Brooks, C. L.; Lee, H. S.; Im, W. Charmm-Gui Ligand Reader and Modeler for Charmm Force Field Generation of Small Molecules. *J. Comput. Chem.* **2017**, *38* (21), 1879-1886.
- 32. Pronk, S.; Pall, S.; Schulz, R.; Larsson, P.; Bjelkmar, P.; Apostolov, R.; Shirts, M. R.; Smith, J. C.; Kasson, P. M.; van der Spoel, D., *et al.* Gromacs 4.5: A High-Throughput and Highly Parallel Open Source Molecular Simulation Toolkit. *Bioinformatics* **2013**, *29* (7), 845-854.
- 33. Martinez, L.; Andrade, R.; Birgin, E. G.; Martinez, J. M. Packmol: A Package for Building Initial Configurations for Molecular Dynamics Simulations. *J. Comput. Chem.* **2009**, *30* (13), 2157-64.
- 34. Israelachvili, J. N. Intermolecular and Surface Forces. 3rd ed.; Academic Press: 2011.
- 35. Shirts, M. R.; Chodera, J. D. Statistically Optimal Analysis of Samples from Multiple Equilibrium States. *J. Chem. Phys.* **2008**, *129* (12).
- 36. Eastoe, J.; Hatzopoulos, M. H.; Dowding, P. J. Action of Hydrotropes and Alkyl-Hydrotropes. *Soft Matter* **2011,** *7* (13), 5917-5925.
- 37. Lin, S. Y.; Lin, Y. Y.; Chen, E. M.; Hsu, C. T.; Kwan, C. C. A Study of the Equilibrium Surface Tension and the Critical Micelle Concentration of Mixed Surfactant Solutions. *Langmuir* **1999**, *15* (13), 4370-4376.
- 38. Chen, L. J.; Lin, S. Y.; Huang, C. C.; Chen, E. M. Temperature Dependence of Critical Micelle Concentration of Polyoxyethylenated Non-Ionic Surfactants. *Colloids Surf., A* **1998**, *135* (1-3), 175-181.

- 39. Patist, A.; Bhagwat, S. S.; Penfield, K. W.; Aikens, P.; Shah, D. O. On the Measurement of Critical Micelle Concentrations of Pure and Technical-Grade Nonionic Surfactants. *J. Surfactants Deterg.* **2000**, *3* (1), 53-58.
- 40. Ghosh, S. K.; Khatua, P. K.; Bhattacharya, S. C. Aggregation of Non Ionic Surfactant Igepal in Aqueous Solution: Fluorescence and Light Scattering Studies. *Int. J. Mol. Sci.* **2003**, *4* (11), 562-571.
- 41. Vishnyakov, A.; Lee, M. T.; Neimark, A. V. Prediction of the Critical Micelle Concentration of Nonionic Surfactants by Dissipative Particle Dynamics Simulations. *J. Phys. Chem. Lett.* **2013**, *4* (5), 797-802.
- 42. Zana, R.; Weill, C. Effect of Temperature on the Aggregation Behavior of Nonionic Surfactants in Aqueous-Solutions. *J. Phys. Lett.* **1985**, *46* (20), 953-960.
- 43. Lebecque, S.; Crowet, J. M.; Nasir, M. N.; Deleu, M.; Lins, L. Molecular Dynamics Study of Micelles Properties According to Their Size. *J. Mol. Graphics Modell.* **2017**, *72*, 6-15.
- 44. Segota, S.; Tezak, D. Spontaneous Formation of Vesicles. *Adv. in Colloid and Interface Sci.* **2006**, *121* (1-3), 51-75.
- 45. Gradzielski, M. Investigations of the Dynamics of Morphological Transitions in Amphiphilic Systems. *Curr. Opin. Colloid Interface Sci.* **2004**, *9* (3-4), 256-263.
- 46. Tummino, P. J.; Gafni, A. Determination of the Aggregation Number of Detergent Micelles Using Steady-State Fluorescence Quenching. *Biophys. J.* **1993**, *64* (5), 1580-1587.
- 47. Jusufi, A.; Panagiotopoulos, A. Z. Explicit- and Implicit-Solvent Simulations of Micellization in Surfactant Solutions. *Langmuir* **2015**, *31* (11), 3283-3292.

- 48. Huang, C. J.; Quinn, D.; Sadovsky, Y.; Suresh, S.; Hsia, K. J. Formation and Size Distribution of Self-Assembled Vesicles. *Proc. Natl. Acad. Sci. U. S. A.* **2017,** *114* (11), 2910-2915.
- Karlsson, M.; Sott, K.; Davidson, M.; Cans, A. S.; Linderholm, P.; Chiu, D.; Orwar, O.
   Formation of Geometrically Complex Lipid Nanotube-Vesicle Networks of Higher-Order
   Topologies. *Proc. Natl. Acad. Sci. U. S. A.* 2002, 99 (18), 11573-11578.
- 50. Karlsson, R.; Karlsson, A.; Orwar, O. Formation and Transport of Nanotube-Integrated Vesicles in a Lipid Bilayer Network. *J. Phys. Chem. B* **2003**, *107* (40), 11201-11207.
- 51. Sekine, Y.; Abe, K.; Shimizu, A.; Sasaki, Y.; Sawada, S.; Akiyoshi, K. Shear Flow-Induced Nanotubulation of Surface-Immobilized Liposomes. *Rsc Adv.* **2012**, *2* (7), 2682-2684.
- 52. Hagendorfer, H.; Kaegi, R.; Parlinska, M.; Sinnet, B.; Ludwig, C.; Ulrich, A. Characterization of Silver Nanoparticle Products Using Asymmetric Flow Field Flow Fractionation with a Multidetector Approach a Comparison to Transmission Electron Microscopy and Batch Dynamic Light Scattering. *Anal. Chem.* **2012**, *84* (6), 2678-2685.
- 53. Panchal, J.; Kotarek, J.; Marszal, E.; Topp, E. M. Analyzing Subvisible Particles in Protein Drug Products: A Comparison of Dynamic Light Scattering (Dls) and Resonant Mass Measurement (Rmm). *AAPS J.* **2014**, *16* (3), 440-451.
- 54. Calzolai, L.; Gilliland, D.; Garcia, C. P.; Rossi, F. Separation and Characterization of Gold Nanoparticle Mixtures by Flow-Field-Flow Fractionation. *J. Chromatogr. A* **2011,** *1218* (27), 4234-4239.
- 55. Karow, A. R.; Gotzl, J.; Garidel, P. Resolving Power of Dynamic Light Scattering for Protein and Polystyrene Nanoparticles. *Pharm. Dev. Technol.* **2015**, *20* (1), 84-89.

- 56. Patel, N. M.; Moore, J. D.; Blackwell, H. E.; Amador-Noguez, D. Identification of unanticipated and novel N-acyl L-homoserine lactones (AHLs) using a sensitive non-targeted LC-MS/MS method. *PloS one* **2016**, *11* (10), e0163469.
- 57. Charlton, T. S.; de Nys, R.; Netting, A.; Kumar, N.; Hentzer, M.; Givskov, M.; Kjelleberg, S. A Novel and Sensitive Method for the Quantification of N-3-Oxoacyl Homoserine Lactones Using Gas Chromatography-Mass Spectrometry: Application to a Model Bacterial Biofilm. *Environ. Microbiol.* **2000**, *2* (5), 530-541.
- 58. Chopp, D. L.; Kirisits, M. J.; Moran, B.; Parsek, M. R. A Mathematical Model of Quorum Sensing in a Growing Bacterial Biofilm. *J. Ind. Microbiol. Biotechnol.* **2002**, *29* (6), 339-346.
- 59. Basu, S.; Gerchman, Y.; Collins, C. H.; Arnold, F. H.; Weiss, R. A Synthetic Multicellular System for Programmed Pattern Formation. *Nature* **2005**, *434* (7037), 1130-1134.
- 60. Soberon-Chavez, G.; Lepine, F.; Deziel, E. Production of Rhamnolipids by Pseudomonas Aeruginosa. *Appl. Microbiol. Biotechnol.* **2005**, *68* (6), 718-725.

# For Table of Contents Use Only:

